Coherent revival of tunneling

Liang-Yan Hsu* and Herschel Rabitz†
Department of Chemistry, Princeton University, Princeton, New Jersey 08544, USA
(Received 12 April 2015; revised manuscript received 23 June 2015; published 8 July 2015)

We introduce a tunneling effect by a driving field, referred to as coherent revival of tunneling (CRT), corresponding to complete tunneling (transmission coefficient = 1) that is revived from the circumstance of total reflection (transmission coefficient ≈ 0) through application of an appropriate perpendicular high-frequency ac field. To illustrate CRT, we simulate electron transport through fish-bone-like quantum-dot arrays by using single-particle Green's functions along with Floquet theory, and we explore the corresponding current-field amplitude characteristics as well as current-polarization characteristics. In regard to the two characteristics, we show that CRT exhibits entirely different features than coherent destruction of tunneling and photon-assisted tunneling. We also discuss two practical conditions for experimental realization of CRT.

DOI: 10.1103/PhysRevB.92.035410 PACS number(s): 03.65.Xp, 05.60.Gg, 72.40.+w, 73.63.Kv

I. INTRODUCTION

Tunneling in a time-dependent field is a fundamental subject in quantum mechanics and has been investigated for more than 50 years [1–10]. Tunneling phenomena by a driving field have been considered in many different contexts in chemistry [3,4,11] and physics, including photon-assisted tunneling (PAT) [1,2,5,10,12–22], coherent destruction of tunneling (CDT) [6,23,24], dynamical localization [9], and coherent quantum ratchets [25,26]. For example, PAT has been widely explored in superconductor-insulator-superconductor tunnel junctions [1,12], semiconductor nanostructures [13,14], quantum dots [15,16], superlattices [17], and molecular junctions [10,18–22]. CDT has been experimentally observed in an Er:Yb-doped glass [7] and in cold atoms within a double-well potential [8].

In this paper, we introduce a phenomenon called coherent revival of tunneling (CRT), in which total transmission can be achieved by an appropriate perpendicular high-frequency ac field. In addition, we show that CRT exhibits current-polarization characteristics completely different from those of PAT as well as current-field amplitude characteristics distinct from those of CDT. To demonstrate CRT, we consider the following device setup, as shown in Fig. 1(a): a quantum-dot array coupled to two electrodes (the source and the drain) and exposed to a laser field. We will analyze light-driven electron transport through quantum-dot arrays based on four different configurations, labeled I–IV in Fig. 1(b). Configuration I is used to demonstrate CDT, while configurations II–IV are used to demonstrate CRT.

II. MODEL AND METHOD

In order to develop the model Hamiltonian, we adopted several approximations, including (i) the lead-dot model, (ii) the nearest-neighbor tight-binding model and the electric dipole approximation for the quantum-dot arrays in a laser field, (iii) a noninteracting electron model for the electrodes, (iv) thermal equilibrium for the electrons in the electrodes, and (v) the wideband limit approximation for the coupling function. These approximations have been extensively employed in previous studies [10,21,23–25,27–30].

In the lead-dot model, the total system Hamiltonian $H(t)$ is decomposed into the dot Hamiltonian $H_{\rm dot}(t)$, the lead Hamiltonian $H_{\rm lead}$, and the dot-lead couplings $H_{\text{dot-lead}}$, i.e., $H(t) = H_{\rm dot}(t) + H_{\rm lead} + H_{\text{dot-lead}}$. For the quantum-dot arrays, we assume that each dot is placed in the x-y plane, the distance between two nearest-neighbor dots is d, and the laser field propagates along the z direction in Fig. 1. Moreover, the dot Hamiltonian is treated within the nearest-neighbor tight-binding model and the electric dipole approximation, i.e.,

$$H_{\rm dot}(t) = \sum_n [E_0 - e\mathbf{r}_n \cdot \mathbf{E}(t)]|n\rangle\langle n| + \sum_{nn'} \Delta_{nn'}|n\rangle\langle n'|, \quad (1)$$

where e is an elementary charge, $|n\rangle$ stands for the orbital on the nth quantum dot at position $\mathbf{r}_n$, E_0 is the on-site energy, $\Delta_{nn'}$ is the coupling between two nearest-neighbor dots, and $\mathbf{E}(t) = \mathbf{E}(t+T)$ is a monochromatic linearly polarized electric field with a period T and angular frequency $\omega = 2\pi/T$. In a practical experimental setup, it is difficult to obtain the same couplings between dots. To model the fluctuation of dot couplings, we assume that $\Delta_{nn'} = \Delta_{n'n} = \Delta_0 + \Delta_1$, where Δ_0 is a constant and Δ_1 is a random variable which describes the variation of coupling strength. The linearly polarized electric field $\mathbf{E}(t)$ has amplitude E and a polarization angle β in the x-y plane, i.e.,

$$\mathbf{E}(t) = E(\cos\beta\hat{\mathbf{e}}_x + \sin\beta\hat{\mathbf{e}}_y)\cos\omega t, \quad (2)$$

where $\hat{\mathbf{e}}_x$ and $\hat{\mathbf{e}}_y$ stand for unit vectors in the x and y directions, respectively.

The two leads are described by a noninteracting electron model, i.e., $H_{\rm lead} = \sum_{lq} \epsilon_{lq}|lq\rangle\langle lq|$, where $|lq\rangle$ stands for the orbital with energy ϵ_{lq} in lead l with mode q, and $l = \mathrm{S}$ and D denote the source and the drain, respectively. In addition, assuming that the electrons in the leads are in thermal equilibrium, their average occupation number can be expressed as the Fermi function $f_l(\epsilon) = (1 + e^{(\epsilon-\mu_l)/k_{\rm B}\theta})^{-1}$ with chemical potential μ_l in lead l at temperature θ. The dot-lead couplings are modeled as

$$H_{\text{dot-lead}} = \sum_q V_{\mathrm{S}q,u}|\mathrm{S}q\rangle\langle u| + V_{\mathrm{D}q,v}|\mathrm{D}q\rangle\langle v| + \text{H.c.}, \quad (3)$$

*lianghsu@princeton.edu
†hrabitz@princeton.edu

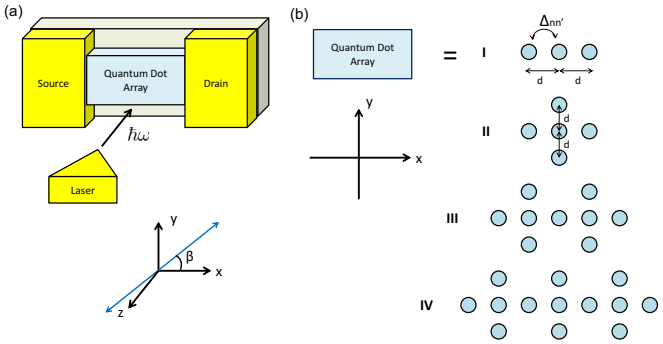

FIG. 1. (Color online) (a) A quantum-dot array coupled to two electrodes (the source and drain electrodes) is exposed to a laser field propagating along the z direction with polarization angle β and frequency ω. Quantum-dot arrays are placed in the x-y plane, and the blue double-headed arrow stands for laser polarization. (b) Quantum-dot arrays I–IV. The distance between two nearest-neighbor quantum dots is d, and the coupling is $\Delta_{nn'}$.

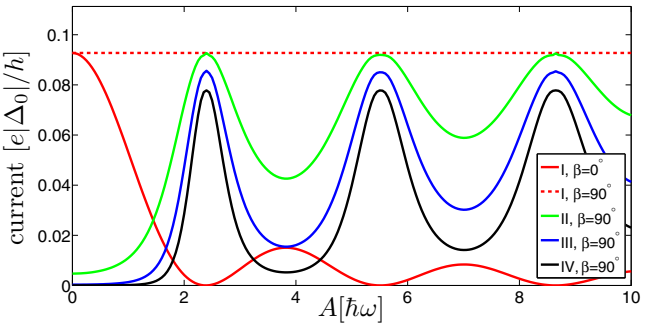

FIG. 2. (Color online) Current-field amplitude characteristics for $V_{SD} = 0.05\Delta_0$, $k_B\theta = 0$, $\Delta_1 = 0$, $\hbar\omega = 10|\Delta_0|$, and $\Gamma = 0.1\Delta_0$, where $A = edE$ is proportional to the field amplitude E. Red solid (dashed) lines show the current through array I in a laser field with a polarization angle $\beta = 0^\circ$ (90°). Green, blue, and black solid lines correspond to currents through arrays II–IV, respectively, in a laser field with a polarization angle $\beta = 90^\circ$.

where $|u\rangle$ ($|v\rangle$) represents dot u (v) coupled to the source (drain) and the element of the coupling function can be expressed as $\Gamma_{l,m}(\epsilon) = 2\pi\sum_q |V_{lq,m}|^2\delta(\epsilon - \epsilon_{lq})$, $(l,m) = (S,u)$ and (D,v). Consider the symmetric coupling and the wide-band limit approximation, which corresponds to $\Gamma_{S,u}(\epsilon) = \Gamma_{D,v}(\epsilon) = \Gamma = \text{const}$. That is, we keep only the imaginary part of the self-energy and set $\Sigma = \frac{-i}{2}(|u\rangle\Gamma\langle u| + |v\rangle\Gamma\langle v|)$ since the real part of the self-energy does not play a crucial role in the analysis.

In a time-periodic field, the time-averaged current can be computed using [10,21,24,25,27–29,31]

$$\bar{I} = \frac{2e}{h}\sum_{k=-\infty}^{+\infty}\int d\epsilon\{T_{DS}^{(k)}(\epsilon)f_S(\epsilon) - T_{SD}^{(k)}(\epsilon)f_D(\epsilon)\}, \quad (4)$$

where $T_{DS}^{(k)}(\epsilon) = \Gamma_{D,v}(\epsilon + k\hbar\omega)\Gamma_{S,u}(\epsilon)|G_{vu}^{(k)}(\epsilon)|^2$ reads the transmission of the tunneling electron from the source to the drain with energy ϵ accompanied by k-photon absorption ($k > 0$) or emission ($k < 0$). The kth component of the retarded Green's function $G_{vu}^{(k)}(\epsilon)$ can be derived from the time-independent infinite-dimensional Floquet eigenvalue matrix equation [10,21,22]. We let $T_{SD}(\epsilon) = \sum_{k=-\infty}^{\infty} T_{SD}^{(k)}(\epsilon)$ and $T_{DS}(\epsilon) = \sum_{k=-\infty}^{\infty} T_{DS}^{(k)}(\epsilon)$; Eq. (4) becomes

$$\bar{I} = \frac{2e}{h}\int_{-\infty}^{\infty} d\epsilon[T_{DS}(\epsilon)f_S(\epsilon) - T_{SD}(\epsilon)f_D(\epsilon)]. \quad (5)$$

In arrays I–IV, the generalized parity symmetry $S_{GP} : (\mathbf{r},t) \to (-\mathbf{r},t + \pi/\omega)$ is satisfied [32], so we have $T_{SD}(\epsilon) = T_{DS}(\epsilon)$, and the transmission coefficient can be defined as $T(\epsilon) = T_{SD}(\epsilon)$ [21]. Equation (5) reduces to a Landauer-type formula.

III. RESULTS AND DISCUSSIONS

Consider the following conditions in the experimental setup. We assume a small applied voltage ($eV_{SD} = 0.05\Delta_0$) and symmetric chemical potentials ($\mu_S = E_0 + eV_{SD}/2$, $\mu_D = E_0 - eV_{SD}/2$, and $E_0 = 0$). Figure 2 shows current-field amplitude characteristics of the triple quantum dots I and the fish-bone-like quantum-dot arrays II–IV. Note that in Figs. 2, 3, and 5, we do not consider variation of coupling strength and set $\Delta_1 = 0$. In array I, the current is strongly suppressed at $A \approx 2.4$, 5.5, and $8.6\hbar\omega$ [corresponding to the roots of Bessel functions of the first kind, i.e., $J_0(\frac{A}{\hbar\omega}) = 0$] in a laser field with $\beta = 0^\circ$, where A is proportional to the field amplitude E ($A = edE$). This phenomenon is the so-called coherent destruction of tunneling, which has been extensively studied [27,30]. On the other hand, the current does not change with A in a laser field with $\beta = 90^\circ$ because $e\mathbf{r}_n \cdot \mathbf{E}(t) = 0$. In addition, $T(\epsilon) \approx 1$ between μ_S and μ_D due to one of the conduction channels at $\epsilon = 0$. Consequently, the magnitude of the current can be estimated as $\bar{I} = \frac{2e}{h}\int d\epsilon T(\epsilon)[f_S(\epsilon) - f_D(\epsilon)] \approx \frac{2e}{h}V_{SD} = 0.1e\Delta_0/h$, which is very close to the numerical result (the red dashed line in Fig. 2).

On the other hand, the fish-bone-like quantum-dot arrays II–IV in a perpendicular laser field ($\beta = 90^\circ$) exhibit entirely different current-field amplitude characteristics; for example, the current reaches the maximum at the roots of the Bessel function, which is in complete contrast to the CDT observed in array I in a parallel laser field ($\beta = 0^\circ$). To understand this feature, we consider the transmission spectra of array II and the corresponding energy levels of the quasistates. The upper and lower bright lines in Fig. 3(a) correspond to the energies of quasistates in Fig. 3(b), indicating that the quasistates provide conduction channels for tunneling electrons. However, the intensity of the transmission spectra along $\epsilon = 0$ changes with the field amplitude A and shows strong transmission suppression at small A. It is intriguing that the quasistates exist but they do not assist in tunneling. The transmission suppression is a manifestation of tunneling with destructive quantum interference (DQI) due to the synergistic effect of resonant states (conduction channels). The synergistic effect of resonant states caused by specific structures in the absence of a driving field has been extensively discussed in the domain of molecular electronics [33–39]. However, as A reaches the roots of the Bessel function, the strong transmission suppression vanishes, and the total transmission is revived (the synergistic effect of the conduction channels disappears, and the conduction channel is revived),

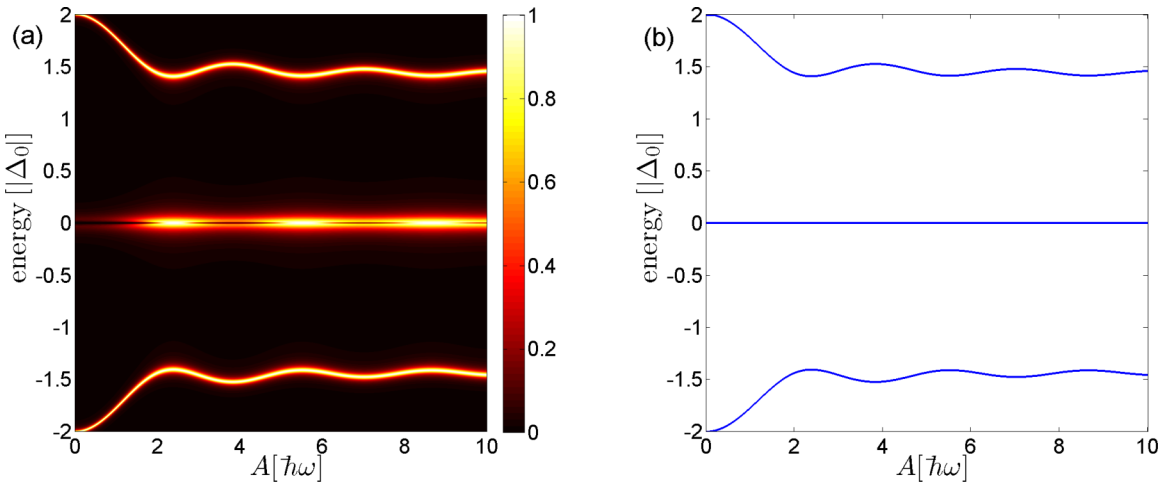

FIG. 3. (Color online) (a) Transmission spectra of array II under laser fields for $E_0 = 0$, $\hbar\omega = 10|\Delta_0|$, $\beta = 90^\circ$, $\Delta_1 = 0$, and $\Gamma = 0.1\Delta_0$, where the color denotes the magnitude of transmission on a linear scale. (b) The energies of the quasistates of array II in the first Brillouin zone ($-\hbar\omega/2 < \epsilon < \hbar\omega/2$).

indicating that the current reaches the local maximum. As a result, we call this phenomenon *coherent revival of tunneling*.

It is interesting that the patterns of quasistate energies in CRT and CDT are completely different (see Fig. 7 in Appendix A). For array II, the energies of the five quasistates in the first Brillouin zone can be solved in the high-frequency approximation ($\hbar\omega \gg \Delta_0$), and they are $-\Delta_0\sqrt{2+2|J_0(\frac{A}{\hbar\omega})|^2}, 0$ (three degenerate states), and $\Delta_0\sqrt{2+2|J_0(\frac{A}{\hbar\omega})|^2}$ (the details can be found in Appendix B). Numerical results also show that the energies of the three degenerate states are insensitive to the field amplitude and the upper and lower lines never intersect at $\epsilon = 0$. In Fig. 3, the suppression and revival of tunneling are independent from the quasistate energies of the three degenerate states. On the contrary, CDT results from the fact that the quasistate energies of array I intersect with each other at the roots of the Bessel function. In addition to numerical results, for the CRT effect, the closed-form expression of the Green's functions also indicates that $T(0) \approx 1$ at $J_0(\frac{A}{\hbar\omega}) = 0$, while $T(0) \approx 0$ at $J_0(\frac{A}{\hbar\omega}) = 1$ (see Appendix B). CRT and CDT show extremely different characteristics in the quasistate energy plot.

The mechanism of CRT can be also understood by the time-averaged effective Hamiltonian in the high-frequency approximation. In a high-frequency field ($\hbar\omega \gg \Delta_0$), we can make a transformation of the Hamiltonian of array II to a rotating frame [40], and the effective coupling in the three dots indicated by the red box in Fig. 4 becomes $\Delta_{\rm eff} = \Delta_{nn'} J_0(\frac{A}{\hbar\omega})$. As $J_0(\frac{A}{\hbar\omega}) = 0$, array II is nearly equivalent to array I, so the tunneling with DQI vanishes, and the current reaches the maximum. In addition, Fig. 2 shows that the maximum current through array II (the green line) almost coincides with the current through array I, which also indicates that array II reduces to array I when $J_0(\frac{A}{\hbar\omega}) = 0$. Based on this assessment, in a high-frequency laser field with $\beta = 90^\circ$ and $J_0(\frac{A}{\hbar\omega}) = 0$, arrays III and IV are equivalent to five and seven linear quantum dots, respectively.

The tunneling effect in a time-dependent field can be also investigated by current-polarization characteristics. For example, one-photon-assisted tunneling exhibits $\overline{I} \propto \cos^2\beta$ [22]; that is, the current reaches the maximum at $\beta = 0^\circ$ and the minimum at $\beta = 90^\circ$. It can be understood that electron tunneling driven by electric-field oscillation is most efficient when the directions of electron tunneling and electric-field oscillation are the same. However, the fish-bone-like quantum-dot arrays show different features in current-polarization amplitude characteristics. Figure 5 shows that the maximum current through arrays II–IV occurs at $\beta = 90^\circ$ (the directions of current and polarization are perpendicular), while the nearly zero current occurs at $\beta = 0^\circ$. The nearly zero current at $\beta = 0^\circ$ originates from CDT, while the maximum current at $\beta = 90^\circ$ results from CRT. Moreover, the width of the current peak in Fig. 5 becomes narrower as the length of the fish-bone structure increases. This feature results from tunneling with DQI enhanced by the repeated cross structures.

In practice, various experimental conditions need to be considered. Here we discuss two of these experimental conditions: (i) variation of coupling strength between the dots and (ii) leakage currents caused by a breakdown electric field. First, it is extremely difficult to obtain the same couplings between dots. In order to model the variation of coupling strength between dots, we assume that Δ_1 is a random variable

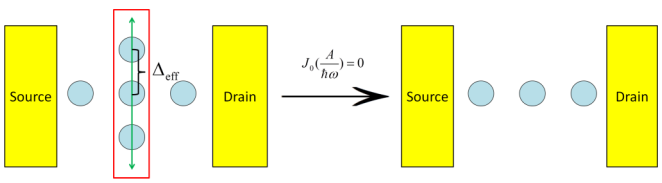

FIG. 4. (Color online) Mechanism of coherent revival of tunneling. Electron transport through array II in a laser field with $\beta = 90^\circ$ (the green double-headed arrow denotes laser polarization). In a high-frequency field, the coupling $\Delta_{nn'}$ in the three dots indicated by the red box can transform into the effective coupling $\Delta_{\rm eff} = \Delta_{nn'} J_0(\frac{A}{\hbar\omega})$, where $J_0(\frac{A}{\hbar\omega})$ is a Bessel function of the first kind. As $J_0(\frac{A}{\hbar\omega}) = 0$, array II is nearly equivalent to array I, and destructive quantum interference caused by the fish-bone-like structure vanishes.

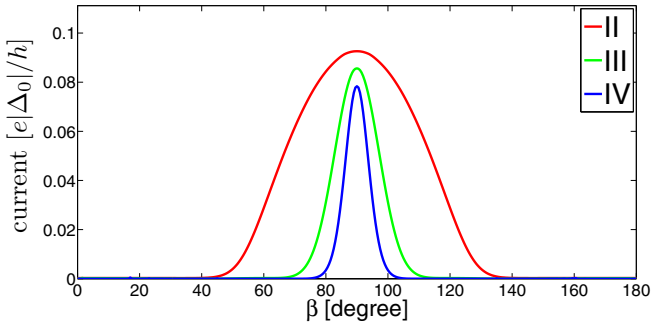

FIG. 5. (Color online) Current-polarization characteristics of arrays II–IV under laser fields for $\hbar\omega = 10|\Delta_0|$, $A = 2.405\hbar\omega$, $\Delta_1 = 0$, and $\Gamma = 0.1\Delta_0$.

and $|\Delta_1| < 0.3\Delta_0$. Figure 6 shows current through array IV with uniform couplings (the red line) and with six sets of random couplings (the black lines). We find that even in the intermediate-frequency regime ($\hbar\omega = 4|\Delta_0|$), the peaks of the red and black lines all still occur close to the roots of the Bessel function, indicating that the feature of CRT is not sensitive to variation of coupling strength, and CRT can be observed in the fish-bone-like quantum-dot arrays with imperfect fabrication. Note that variation of coupling strength may enhance the maximum current due to the breaking of the generalized parity symmetry. As the generalized parity symmetry no longer holds, zero-bias current can be driven by a time-periodic field, leading to current enhancement or suppression [32]. Second, when the strong electric-field oscillation is parallel to the direction of tunneling current, a source-to-drain leakage current may occur due to electric-field breakdown of the quantum dots. (The breakdown electric field of excellent insulators such as Al_2O_3 is about 1 V/nm [41].) However, for CRT, a source-to-drain leakage current can be avoided because the electric-field oscillation is perpendicular to the direction of the source-to-drain current.

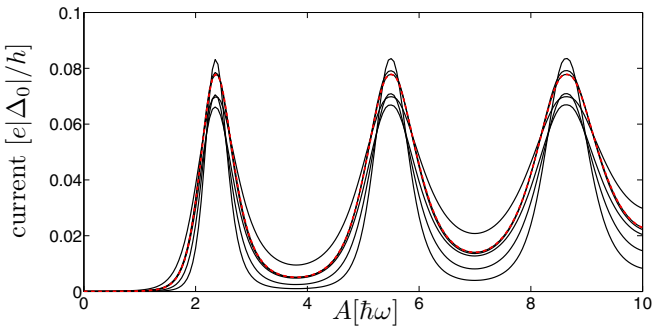

FIG. 6. (Color online) Current-field amplitude characteristics of array IV for $V_{SD} = 0.05\Delta_0$, $k_B\theta = 0$, $\hbar\omega = 4|\Delta_0|$, and $\Gamma = 0.1\Delta_0$. The red line corresponds to current through array IV with uniform couplings ($\Delta_1 = 0$), while the black lines correspond to current through array IV with six sets of random couplings ($|\Delta_1| < 0.3\Delta_0$).

IV. CONCLUSION

To summarize, we have presented the concepts of CRT and discussed the corresponding current-field amplitude and current-polarization characteristics. The results imply that the fish-bone-like quantum-dot arrays are good candidates for the observation of CRT. We would like emphasize the distinctions between CRT and CDT: (i) CRT and CDT occur in a laser field with polarization angles 90° and 0°, respectively. (ii) As $J_0(\frac{A}{\hbar\omega}) = 0$, CRT exhibits current enhancement (complete tunneling), while CDT shows current suppression. (iii) No energy-level crossing of quasistates occurs in CRT. For a practical experimental setup, we find that CRT is not sensitive to reasonable variation of coupling strength between dots. Moreover, the condition $\beta = 90°$ for CRT can avoid unexpected tunneling mechanisms such as source-to-drain leakage currents. Note that the Coulomb interaction and spin-orbit coupling may influence the CRT effect. In this study, we explored the CRT effect in the single-electron tunneling regime (the low-bias condition). In this condition, Coulomb interaction should not play a crucial role [42,43]. In addition, according to a previous study [44], the spin-orbit interaction is much smaller than Δ_0 in double quantum dots. As a result, it is reasonable to neglect the spin-orbit interaction in order to facilitate the theoretical analysis and provide a clear explanation of the CRT mechanism. We hope that this study motivates additional investigations into CRT as well as other novel tunneling effects driven by time-dependent fields in various contexts.

ACKNOWLEDGMENTS

The authors thank Dr. T.-S. Ho for useful discussions. L.-Y. Hsu acknowledges support by the NSF (Grant No. CHE-1058644) and the Program in Plasma Science and Technology at Princeton University. H.R. acknowledges partial support from the ARO (Grant No. W911NF-13-1-0237) for the control principles and DOE (Grant No. DE-FG02-02ER15344) for the modeling.

APPENDIX A: TRANSMISSION SPECTRUM AND QUASI-STATE ENERGY PLOT OF I

The patterns of transmission functions and quasistate energies in CRT and CDT are completely different. To compare the difference between CRT and CDT, we demonstrate the transmission spectra and the quasistate energies of array I, as shown in Figs. 7(a) and 7(b). The bright lines in Fig. 7(a) correspond to the energies of quasistates in Fig. 7(b). When the three quasistate curves in Fig. 7(b) cross each other, the effective couplings between dots become zero, leading to zero transmission in Fig. 7(a). This is the origin of CDT.

APPENDIX B: CLOSED-FORM EXPRESSION FOR QUASISTATE ENERGY AND GREEN'S FUNCTION OF ARRAY II

In order to understand the origin of coherent revival of tunneling (CRT) and the curves of the quasistate energies in Fig. 3, we solve the time-dependent Schrödinger equation of

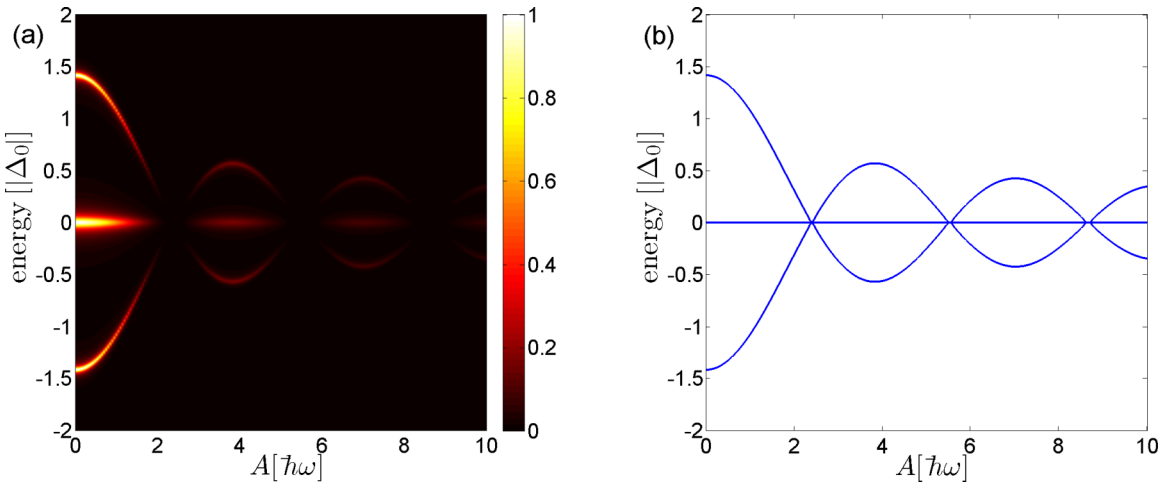

FIG. 7. (Color online) (a) Transmission spectra of array I under laser fields for $E_0 = 0$, $\hbar\omega = 10|\Delta_0|$, $\beta = 0^\circ$, $\Delta_1 = 0$, and $\Gamma = 0.1\Delta_0$, where the colors denote the magnitude of transmission on a linear scale. (b) The energies of the quasistates of array I in the first Brillouin zone ($-\hbar\omega/2 < \epsilon < \hbar\omega/2$). As $J_0(\frac{A}{\hbar\omega}) = 0$, the three quasistate energy curves cross each other, and the transmission becomes zero at $A \approx 2.40$, 5.52, and $8.65\hbar\omega$, leading to coherent destruction of tunneling.

array II in the high-frequency limit. According to Eqs. (1) and (2), the Hamiltonian of system II in a laser field with the polarization angle $\beta = 90^\circ$ is

$$H_{\rm II}(t) = \begin{array}{c} \\ \langle 1| \\ \langle 2| \\ \langle 3| \\ \langle 4| \\ \langle 5| \end{array} \begin{array}{c} \begin{array}{ccccc} |1\rangle & |2\rangle & |3\rangle & |4\rangle & |5\rangle \end{array} \\ \begin{pmatrix} E_0 & \Delta_0 & 0 & 0 & 0 \\ \Delta_0 & E_0 & \Delta_0 & \Delta_0 & \Delta_0 \\ 0 & \Delta_0 & E_0 & 0 & 0 \\ 0 & \Delta_0 & 0 & E_0 + A\cos(\omega t) & 0 \\ 0 & \Delta_0 & 0 & 0 & E_0 - A\cos(\omega t) \end{pmatrix} \end{array}, \tag{B1}$$

where $|n\rangle$ stands for the orbital on the nth quantum dot (see Fig. 8) and $A = edE$. Note that for simplicity we adopt $\Delta_{n,n'} = \Delta_0$.

System II is coupled to the two electrodes, and the effect of the electrodes can be modeled as the self-energy term $\Sigma = \frac{-i}{2}(|1\rangle\Gamma\langle 1| + |3\rangle\Gamma\langle 3|)$, where Γ is a coupling function. To get the closed-form expression of the quasistate energies, we neglect the contribution of the self-energy since $\Gamma \ll \Delta_0$, i.e., set $\Gamma = 0$, and transform the Hamiltonian in Eq. (B1) into a rotating frame,

$$\begin{aligned} H_{\rm II}^{\rm rot}(t) &= U_{\rm rot}^\dagger(t) H_{\rm II}(t) U_{\rm rot}(t) - i\hbar U_{\rm rot}^\dagger(t)\frac{dU_{\rm rot}(t)}{dt} \\ &= \begin{pmatrix} E_0 & \Delta_0 & 0 & 0 & 0 \\ \Delta_0 & E_0 & \Delta_0 & \Delta_0 \exp\left[-i\frac{A}{\hbar\omega}\sin(\omega t)\right] & \Delta_0 \exp\left[i\frac{A}{\hbar\omega}\sin(\omega t)\right] \\ 0 & \Delta_0 & E_0 & 0 & 0 \\ 0 & \Delta_0 \exp\left[i\frac{A}{\hbar\omega}\sin(\omega t)\right] & 0 & E_0 & 0 \\ 0 & \Delta_0 \exp\left[-i\frac{A}{\hbar\omega}\sin(\omega t)\right] & 0 & 0 & E_0 \end{pmatrix}, \end{aligned} \tag{B2}$$

where

$$U_{\rm rot}(t) = \begin{pmatrix} 1 & 0 & 0 & 0 & 0 \\ 0 & 1 & 0 & 0 & 0 \\ 0 & 0 & 1 & 0 & 0 \\ 0 & 0 & 0 & \exp\left[-i\frac{A}{\hbar\omega}\sin(\omega t)\right] & 0 \\ 0 & 0 & 0 & 0 & \exp\left[i\frac{A}{\hbar\omega}\sin(\omega t)\right] \end{pmatrix}. \tag{B3}$$

By using $e^{ia\sin(b)} = \sum_{m=-\infty}^{\infty} J_m(a)e^{imb}$ and the high-frequency approximation, we can derive the time-averaged effective Hamiltonian

$$\overline{H}_{\rm II}^{\rm rot} = \begin{pmatrix} E_0 & \Delta_0 & 0 & 0 & 0 \\ \Delta_0 & E_0 & \Delta_0 & \Delta_0 J_0\left(\frac{A}{\hbar\omega}\right) & \Delta_0 J_0\left(\frac{A}{\hbar\omega}\right) \\ 0 & \Delta_0 & E_0 & 0 & 0 \\ 0 & \Delta_0 J_0\left(\frac{A}{\hbar\omega}\right) & 0 & E_0 & 0 \\ 0 & \Delta_0 J_0\left(\frac{A}{\hbar\omega}\right) & 0 & 0 & E_0 \end{pmatrix}. \tag{B4}$$

The quasistate energies and their corresponding eigenvectors can be solved from the effective matrix equation

$$\sum_n \langle n'|\overline{H}_{\rm II}^{\rm rot}|n\rangle\phi_{n\nu} = q_\nu\phi_{n'\nu}. \tag{B5}$$

From Eqs. (B4) and (B5), as $E_0 = 0$, we can derive the quasistate energies $q_1 = -\Delta_0\sqrt{2+2|J_0(\frac{A}{\hbar\omega})|^2}$, $q_2{=}q_3{=}q_4{=}0$ (three degenerate states), and $q_5 = \Delta_0\sqrt{2+2|J_0(\frac{A}{\hbar\omega})|^2}$. q_1 and q_5 correspond to the lower and upper curves in Fig. 3(b), respectively. q_2, q_3, and q_4 correspond to the line along $\epsilon = 0$ in Fig. 3(b). Moreover, as $A = 0$, we can derive $J_0(\frac{A}{\hbar\omega}) = 1$ and $q_1 = -q_5 = -2\Delta_0$. On the other hand, when $A \to \infty$ or $\frac{A}{\hbar\omega}$ satisfies the roots of the Bessel function $[J_0(\frac{A}{\hbar\omega}) = 0]$, we can obtain $q_1 = -q_5 = -\sqrt{2}\Delta_0$. The two results are in agreement with the behavior of the curves in Fig. 3(b).

In the zero-bias limit, the time-averaged current can be approximated as $\overline{I} \approx \frac{2e}{h}T(\mu)V_{\rm SD} = \frac{2e}{h}T(0)V_{\rm SD}$, where $\mu = 0$ is the chemical potential of the electrodes and $V_{\rm SD}$ is the source-drain voltage. The transmission coefficient $T(\epsilon)$ and the retarded Green's function $G^{\rm R}_{nn'}(\epsilon)$ for a tunneling electron with energy ϵ can be computed via

$$T(\epsilon) = \Gamma^2\left|G^{\rm R}_{nn'}(\epsilon)\right|^2, \tag{B6}$$

$$G^{\rm R}_{nn'}(\epsilon) = \sum_\nu \frac{\phi_{n\nu}\phi_{n'\nu}}{\epsilon - q_\nu}, \tag{B7}$$

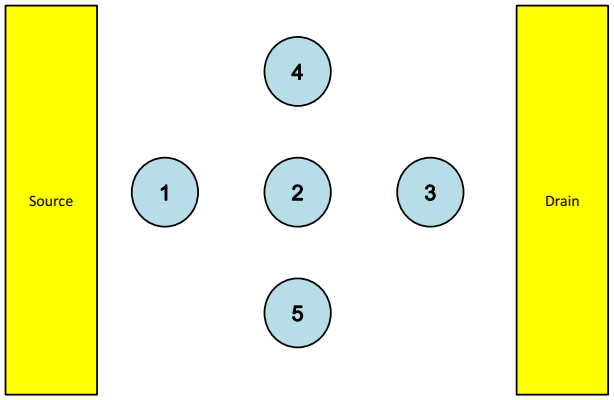

FIG. 8. (Color online) Fish-bone-like quantum-dot array II. The numbers denote the nth quantum dot, e.g., 1 stands for the first quantum dot.

where n and n' correspond to the dots connected to the electrodes. For system II, n and $n' = 1$ or 3.

To compute $T(\epsilon)$ and $G^{\rm R}_{nn'}(\epsilon)$, the self-energy contributed from the electrodes has to be considered. q_ν and $\phi_{n\nu}$ in Eq. (B7) can be solved by

$$\sum_n \langle n'|\overline{H}_{\rm II}^{\rm rot} + \Sigma|n\rangle\phi_{n\nu} = q_\nu\phi_{n'\nu}. \tag{B8}$$

As $\Gamma \neq 0$, the closed forms of q_ν and $\phi_{n\nu}$ are very complicated. However, when $\Gamma \ll \Delta_0$, the quasistate energies can be approximately expressed as $q_1 \approx -\Delta_0\sqrt{2+2|J_0(\frac{A}{\hbar\omega})|^2}$, $q_2 \approx q_3 \approx q_4 \approx 0$, and $q_5 \approx \Delta_0\sqrt{2+2|J_0(\frac{A}{\hbar\omega})|^2}$. The asymptotic values of q_ν and $\phi_{n\nu}$ for $J_0(\frac{A}{\hbar\omega}) = 1$ and 0 are listed in Table I. The sum of eigenvalues is equal to the trace of $\overline{H}_{\rm II}^{\rm rot} + \Sigma$, i.e., $\sum_n \langle n|\overline{H}_{\rm II}^{\rm rot} + \Sigma|n\rangle = -i\Gamma$. Note that in Table I we show only the real part of $\phi_{n\nu}$ since $\mathrm{Re}(\phi_{n\nu}) \gg \mathrm{Im}(\phi_{n\nu})$.

According to Table I, when $J_0(\frac{A}{\hbar\omega}) = 1$, we can derive

$$G^{\rm R}_{13}(0) = \sum_\nu \frac{\phi_{1\nu}\phi_{3\nu}}{-q_\nu} = \frac{-i\Gamma}{128\Delta_0^2 + \frac{\Gamma^2}{2}} \approx 0, \tag{B9}$$

which indicates that $T(0) \approx 0$ and the time-averaged current is nearly zero in the absence of a laser field. This result is intriguing because (i) the state $\nu = 4$ has no contribution to transmission and (ii) the synergistic effect of the states $\nu = 2$ and 3 leads to zero transmission. In other words, the existence of the states in a conductor does not guarantee that they can act as conduction channels.

For $J_0(\frac{A}{\hbar\omega}) = 0$, we can derive

$$G^{\rm R}_{13}(0) = \sum_\nu \frac{\phi_{1\nu}\phi_{3\nu}}{-q_\nu} = \frac{-i\Gamma}{16\Delta_0^2 + \frac{\Gamma^2}{2}} + \frac{i}{\Gamma} \approx \frac{i}{\Gamma}. \tag{B10}$$

TABLE I. The asymptotic values of q_ν and $\phi_{n\nu}$ for $\Gamma \neq 0$ and $\Gamma \ll \Delta_0$.

	$J_0(\frac{A}{\hbar\omega}) = 1$			$J_0(\frac{A}{\hbar\omega}) = 0$		
ν	q_ν	$\phi_{1\nu}$	$\phi_{3\nu}$	q_ν	$\phi_{1\nu}$	$\phi_{3\nu}$
1	$-2\Delta_0 - i\Gamma/8$	$\frac{1}{2\sqrt{2}}$	$\frac{1}{2\sqrt{2}}$	$-\sqrt{2}\Delta_0 - i\Gamma/4$	1/2	1/2
2	$-i\Gamma/2$	$\frac{1}{\sqrt{2}}$	$-\frac{1}{\sqrt{2}}$	$-i\Gamma/2$	$\frac{1}{\sqrt{2}}$	$-\frac{1}{\sqrt{2}}$
3	$-i\Gamma/4$	1/2	1/2	0	0	0
4	0	0	0	0	0	0
5	$2\Delta_0 - i\Gamma/8$	$\frac{1}{2\sqrt{2}}$	$\frac{1}{2\sqrt{2}}$	$\sqrt{2}\Delta_0 - i\Gamma/4$	1/2	1/2

Substituting Eq. (B10) into Eqs. (B6) and (B7), one can derive $T(0) \approx 1$, and the current reaches the maximum. In addition, as $J_0(\frac{A}{\hbar\omega}) = 0$, dots $|4\rangle$ and $|5\rangle$ are decoupled from the other dots. Consequently, the synergistic effect of the states $\nu = 2$ and 3 vanishes, and the state $\nu = 2$ becomes an efficient conduction channel. This is the origin of CRT.

[1] A. H. Dayem and R. J. Martin, Phys. Rev. Lett. **8**, 246 (1962).
[2] P. K. Tien and J. P. Gordon, Phys. Rev. **129**, 647 (1963).
[3] Y. Teranishi and H. Nakamura, Phys. Rev. Lett. **81**, 2032 (1998).
[4] Y. Teranishi and H. Nakamura, J. Chem. Phys. **111**, 1415 (1999).
[5] C. A. Stafford and N. S. Wingreen, Phys. Rev. Lett. **76**, 1916 (1996).
[6] F. Grossmann, T. Dittrich, P. Jung, and P. Hänggi, Phys. Rev. Lett. **67**, 516 (1991).
[7] G. Della Valle, M. Ornigotti, E. Cianci, V. Foglietti, P. Laporta, and S. Longhi, Phys. Rev. Lett. **98**, 263601 (2007).
[8] E. Kierig, U. Schnorrberger, A. Schietinger, J. Tomkovic, and M. K. Oberthaler, Phys. Rev. Lett. **100**, 190405 (2008).
[9] M. Yamaki, H. Mineo, Y. Teranishi, M. Hayashi, Y. Fujimura, H. Nakamura, and S.-H. Lin, J. Phys. Chem. Lett. **5**, 2044 (2014).
[10] L.-Y. Hsu and H. Rabitz, Phys. Rev. Lett. **109**, 186801 (2012).
[11] H. Nakamura and G. Mil'nikov, *Quantum Mechanical Tunneling in Chemical Physics* (CRC Press, Boca Raton, FL, 2013).
[12] P. L. Richards, T. M. Shen, R. E. Harris, and F. L. Lloyd, Appl. Phys. Lett. **36**, 480 (1980).
[13] M. Wagner, Phys. Rev. A **51**, 798 (1995).
[14] L. Arrachea and M. Moskalets, Phys. Rev. B **74**, 245322 (2006).
[15] L. P. Kouwenhoven, S. Jauhar, J. Orenstein, P. L. McEuen, Y. Nagamune, J. Motohisa, and H. Sakaki, Phys. Rev. Lett. **73**, 3443 (1994).
[16] R. H. Blick, R. J. Haung, D. W. van der Weide, K. von Klitzing, and K. Eberl, Appl. Phys. Lett. **67**, 3924 (1995).
[17] P. S. S. Guimaraes, B. J. Keay, J. P. Kaminski, S. J. Allen, P. F. Hopkins, A. C. Gossard, L. T. Florez, and J. P. Harbison, Phys. Rev. Lett. **70**, 3792 (1993).
[18] A. Keller, O. Atabek, M. Ratner, and V. Mujica, J. Phys. B **35**, 4981 (2002).
[19] A. Tikhonov, R. D. Coalson, and Y. Dahnovsky, J. Chem. Phys. **116**, 10909 (2002).
[20] A. Tikhonov, R. D. Coalson, and Y. Dahnovsky, J. Chem. Phys. **117**, 567 (2002).
[21] L.-Y. Hsu, D. Xie, and H. Rabitz, J. Chem. Phys. **141**, 124703 (2014).
[22] L.-Y. Hsu and H. Rabitz, arXiv:1401.4222.
[23] T.-S. Ho, S.-H. Hung, H.-T. Chen, and Shih-I Chu, Phys. Rev. B **79**, 235323 (2009).
[24] S. Camalet, S. Kohler, and P. Hänggi, Phys. Rev. B **70**, 155326 (2004).
[25] J. Lehmann, S. Kohler, P. Hänggi, and A. Nitzan, Phys. Rev. Lett. **88**, 228305 (2002).
[26] T. Salger, S. Kling, T. Hecking, C. Geckeler, L. Morales-Molina, and M. Weitz, Science **326**, 1241 (2009).
[27] S. Camalet, J. Lehmann, S. Kohler, and P. Hänggi, Phys. Rev. Lett. **90**, 210602 (2003).
[28] L. E. F. Foa Torres, Phys. Rev. B **72**, 245339 (2005).
[29] L. E. F. Foa Torres, P. M. Perez-Piskunow, C. A. Balseiro, and G. Usaj, Phys. Rev. Lett. **113**, 266801 (2014).
[30] L. Chen, T. Hansen, and I. Franco, J. Phys. Chem. C **118**, 20009 (2014).
[31] G. Stefanucci, S. Kurth, A. Rubio, and E. K. U. Gross, Phys. Rev. B **77**, 075339 (2008).
[32] J. Lehmann, S. Kohler, and P. Hänggi, J. Chem. Phys. **118**, 3283 (2003).
[33] S. Sautet and C. Joachim, Chem. Phys. Lett. **153**, 511 (1988).
[34] D. M. Cardamone, C. A. Stafford, and S. Mazumder, Nano Lett. **6**, 2422 (2006).
[35] S. H. Ke and W. T. Yang, Nano Lett. **8**, 3257 (2008).
[36] L.-Y. Hsu and B.-Y. Jin, Chem. Phys. **355**, 177 (2009).
[37] Y. Tsuji, A. Staykov, and K. Yoshizawa, J. Am. Chem. Soc. **133**, 5955 (2011).
[38] L.-Y. Hsu, E. Y. Li, and H. Rabitz, Nano Lett. **13**, 5020 (2013).
[39] G. C. Solomon, D. Q. Andrews, R. H. Goldsmith, T. Hansen, M. R. Wasielewski, R. P. Van Duyne, and M. A. Ratner, J. Am. Chem. Soc. **130**, 17301 (2008).
[40] S. Ashhab, J. R. Johansson, A. M. Zagoskin, and F. Nori, Phys. Rev. A **75**, 063414 (2007).
[41] H. C. Lin, P. D. Ye, and G. D. Wilk, Appl. Phys. Lett. **87**, 182904 (2005).
[42] W. G. van der Wiel, S. De Franceschi, J. M. Elzerman, T. Fujisawa, S. Tarucha, and L. P. Kouwenhoven, Rev. Mod. Phys. **75**, 1 (2002).
[43] M. Di Ventra, *Electron Transport in Nanoscale Systems* (Cambridge University Press, Cambridge, UK, 2008).
[44] S. Nadj-Perge, S. M. Frolov, J. W. W. van Tilburg, J. Danon, Yu. V. Nazarov, R. Algra, E. P. A. M. Bakkers, and L. P. Kouwenhoven, Phys. Rev. B **81**, 201305(R) (2010).